Atomistic Modelling of Crack-Inclusion Interaction in Graphene

M. A. N. Dewapriya[1,2], S. A. Meguid[1,*] and R. K. N. D. Rajapakse[2]
[1] Mechanics and Aerospace Design Laboratory, Department of Mechanical and Industrial Engineering, University of Toronto, Toronto, Canada
[2] School of Engineering Science, Simon Fraser University, Burnaby, Canada
[*]Corresponding author. Email: meguid@mie.utoronto.ca

Abstract

In continuum fracture mechanics, it is well established that the presence of crack near an inclusion leads to a significant change in the crack-tip stress field. However, it is unclear how atomistic crack-inclusion interaction manifests itself at the nanoscale where the continuum description of matter breaks down. In this work, we conducted molecular dynamics simulations to investigate the interactions of an atomic-scale boron nitride inclusion with an edge crack in a graphene sheet. Numerical simulations of nanoscale tensile tests were obtained for graphene samples containing an edge crack and a circular inclusion. Stress analysis of the samples show the complex nature of the stress state at the crack-tip due to the crack-inclusion interaction. Results reveal that the inclusion results in an increase (amplification) or a decrease (shielding) of the crack-tip stress field depending on the location of the inclusion relative to the crack-tip. Our numerical experiments unveil that inclusions of specific locations could lead to a reduction in the fracture resistance of graphene. Results of the crack-inclusion interaction study were compared with the corresponding results of crack-hole interaction problem. The study also provides an insight into the applicability of well-established continuum crack-microdefect interaction models for the corresponding atomic scale problems.

Keywords: Graphene; fracture; inclusion; nanomechanics; crack-tip stress field; molecular dynamics.

1. Introduction

Nanoscale defects such as cracks, vacancies and impurities are difficult to avoid in fabrication of graphene based nano-devices [1–5]. Inclusions and vacancies may be created in graphene for functional reasons and property enhancement [6–11]. It is critically important to examine the effects of these inhomogeneities on the failure and mechanical behavior of graphene. The classical continuum mechanics establishes that inclusions in close proximity to a crack-tip can lead to a considerable change in the crack-tip stress field [12–16]. However, it is unclear how the crack-inclusion interaction manifests itself at the nanoscale. Considering the fact that the concepts of continuum mechanics have limited applicability at the nanoscale [17–23], a comprehensive atomistic study on this subject is particularly important. Earlier, Dewapriya and Meguid conducted atomic simulations on the interaction between a crack and an atomic hole located near its tip under mode I loading [24,25]. In the current work, we explore the crack-inclusion interactions focusing on the influence of interactions between an edge crack in a graphene sheet and an arbitrarily located inhomogeneity of boron nitride (known hereafter as BN inclusions) on the crack-tip stress field and the fracture resistance of graphene. In the view of its ability to cover a larger range of crack-inhomogeneity interaction problems, the current work invokes greater interest among engineers and scientists. For example, the current problem reduces to the limiting case of a crack-hole interaction when the properties of the inclusion reduce to zero. In addition, the study provides an important insight into the applicability of the corresponding continuum mechanics based computational tools for the atomic scale crack-inclusion interaction problems.

Besides having a similar lattice structure of graphene, BN possesses electromechanical properties which are quite comparable to those of graphene [26,27]. In contrast to the

zero-bandgap semimetal nature of graphene, BN is a finite-bandgap semiconductor [28,29]. The similarity of the lattice structures of graphene and BN allows the construction of graphene-BN heterostructures with unique electronic and magnetic properties [30,31]. More importantly, the physical properties of the graphene-BN heterostructures can be effectively tailored by the relative domain size of each material [32,33], which is quite beneficial for numerous advanced potential applications in various fields of engineering [6–8]. For these advanced applications, a solid understanding of the mechanical behavior of graphene-BN heterostructures is vital. Especially, the fracture characteristics of such a hybrid structure is critically important, because both graphene and BN have relatively low fracture toughness compared to other commonly used engineering materials [34].

Most of the recent atomistic simulation efforts have focused on characterizing the electromechanical behaviors of graphene-BN heterostructures [33,35–37] and their interfaces [34,38,39] without investigating the highly complex stress state of a crack interacting with an inclusion. A comprehensive molecular dynamics (MD) investigation of the nanoscale crack-inclusion interaction could provide a significant insight into the rich atomistic mechanisms of 2D materials. Notably, many existing MD studies that are concerned with the fracture characteristics of graphene have focused on the central crack problem mostly due to the convenience of implementing periodic boundary conditions in MD. Our MD simulations of graphene samples containing an edge crack and an atomic inclusion reveal the complex stress states of the hybrid material system due to the nanoscale crack-inclusion interaction. Furthermore, our numerical experiments unveil that inclusions of specific locations would lead to a reduction in the fracture resistance of graphene.

2. Molecular Dynamics Simulations

The planar dimensions of the simulated hybrid graphene-BN samples considered in our studies were 60 nm × 60 nm, and the length of the edge crack was taken to be 10 nm. The domain boundaries of selected simulation samples do not fall within the process zone [25,40], and the crack length of 10 nm was selected in order to avoid the crack length dependency of the simulation results [41,42]. Figure 1(a) shows a typical simulation sample of graphene containing a circular BN inclusion and an edge crack. In view of the fact that both (a) graphene and BN have a similar bond structure and (b) C-C and B-N bond lengths are 1.44 Å [43], the BN inclusion was modeled by appropriately replacing the corresponding carbon atoms in graphene by boron and nitrogen atoms. The edge crack was created by removing carbon atoms in graphene accordingly. The origin of the Cartesian coordinate system is taken at the tip of the crack. The diameter of the inclusion was assumed to be $2c$. To avoid weak crack-inclusion interaction, the inclusion must be located very close to the crack-tip and it should have a significantly large diameter to have a notable influence on the crack-tip stress field. Therefore, the diameter $2c$ was taken to be 3.6 nm. The interference distance between the tip of the crack and the center of the inclusion is r. The inclination angle between the x-axis and the line joining the tip of the crack and the center of the inclusion is θ. It should be noted that the sample containing a zigzag crack is loaded along the armchair direction and the sample containing an armchair crack is loaded along the zigzag direction. For a set of simulations, the inclusion was replaced by an atomic hole with similar dimensions to the inclusion in order to investigate the crack-hole interaction, which is the lower bound of the crack-inclusion interaction problem.

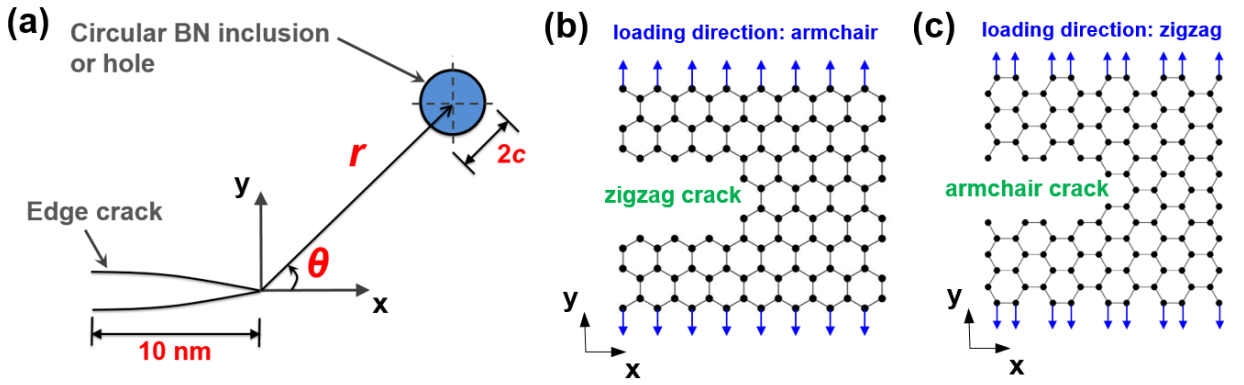

Figure 1 Molecular dynamics models: (**a**) a typical sample of graphene containing an edge crack and a circular BN inclusion. (**b**) and (**c**) show the atomic configurations of zigzag and armchair crack-tips, respectively. Blue arrows indicate the loading direction.

Numerical uniaxial tensile tests of graphene samples were conducted using LAMMPS MD simulator [44]. It should be noted that the BN inclusion is covalently bonded to the surrounding graphene sheet and all the bonded interactions are modelled using the Tersoff potential [43]. According to the Tersoff potential, the energy stored in a bond between atom *i* and atom *j* can be expressed as

$$E_{ij} = f^C(r_{ij})\left[f^R(r_{ij}) + b_{ij} f^A(r_{ij})\right] \tag{1}$$

where $f_{ij}^R(r_{ij})$ and $f_{ij}^A(r_{ij})$ are the repulsive and attractive potentials, respectively; b_{ij} is the bond order term, which modifies the attractive potential according to the local bonding environment; r_{ij} is the distance between the atoms *i* and *j*; the cut-off function $f_{ij}^C(r_{ij})$ limits the interatomic interactions to the nearest neighbors, and it is expressed as

$$f^C(r_{ij}) = \begin{cases} 1, & r_{ij} < R_{ij} \\ \frac{1}{2} + \frac{1}{2}\cos\left[\frac{\pi(r_{ij}-R_{ij})}{(S_{ij}-R_{ij})}\right], & R_{ij} < r_{ij} < S_{ij} \\ 0, & S_{ij} < r_{ij} \end{cases}, \tag{2}$$

where R_{ij} and S_{ij} are the cut-off radii. The values of cut-off radii are defined considering the first and the second nearest neighboring distances of relevant atomic structures. This cut-off radii, however, causes a non-physical strain hardening in the stress-strain curves [45]. Similar strain hardening phenomenon exists in other Tersoff type potentials such as the REBO potential [46–48]. In order to eliminate this spurious strain hardening, modified cut-off radii (ranging from 1.9 Å to 2.2 Å) have been used in the literature [41,49,50]. A truncated cut-off function $f_t(r_{ij})$, given in Eq. (3) [45,51], was used in the current study.

$$f_t(r_{ij}) = \begin{cases} 1, & r_{ij} < R \\ 0, & r_{ij} > R \end{cases}, \tag{3}$$

where the value of R is selected to be 2 Å. Similar truncated cut-off functions have been widely used for fracture simulations of graphene [52–54].

At the beginning of all MD simulations, energy minimization of the simulation samples was conducted by using the conjugate gradient algorithm. Then, the samples were allowed to reach the equilibrium configuration over 25 ps under a time step of 0.5 fs. All the simulations were conducted with the canonical (NVT) ensemble, where temperature was kept constant at 300 K using Noše-Hoover thermostat. Initial displacement perturbations (~0.01 Å) along the x-, y-, and z-directions were imposed on the atoms to facilitate reaching their equilibrium configuration [55]. After the graphene sample reached equilibrium, those were subjected to strain along the y-direction (ε_{yy}) at a rate of 0.001 ps^{-1}. In order to accurately simulate the uniaxial tensile test, the sample was allowed to relax along the direction perpendicular to the loading direction (i.e. x-direction) during the simulation.

Virial theorem was used for the calculation of atomic stress [56,57]. The averaged virial stress tensor, σ_{ij}, is defined as follows:

$$\sigma_{ij} = \frac{1}{V}\sum_{\alpha}\left[\frac{1}{2}\sum_{\beta=1}^{N}\left(R_i^{\beta} - R_i^{\alpha}\right)F_j^{\alpha\beta} - m^{\alpha}v_i^{\alpha}v_j^{\alpha}\right] \quad (4)$$

where i and j are the directional indices (i.e. x, y, and z); α is a number assigned to an atom and β is a number assigned to neighboring atoms of α; R_i^{β} is the position of atom β along the direction i; $F_j^{\alpha\beta}$ is the force on atom α due to atom β along the direction j; m^{α} and v^{α} are the mass and the velocity of atom α, respectively; V is the total volume. In volume calculation, the thickness of graphene and BN was assumed to be 3.4 Å [58,59].

Time averaging of the virial stress over a sufficiently long period is necessary in order to obtain converged stresses [56]. When obtaining atomic stresses of individual atoms, the graphene samples were initially subjected to a strain of 1% at a strain rate of 0.001 ps^{-1} (over 20,000 time steps). At this particular strain, the graphene samples were equilibrated for 50,000 time steps and computed the stresses of individual atoms at each time step. Following that, the computed atomic stresses were averaged over the last 30,000 time steps of the equilibration period in order to obtain the average stresses. Visual Molecular Dynamics package [60] was used to visualize deformations of the hybrid graphene-BN samples.

3. Results and discussion

3.1 *Validation of molecular dynamics results*

In this section, MD simulations of the current study were validated by evaluating Young's modulus and the fracture stress of pristine graphene and BN samples and comparing the results with those existing in the literature. Figure 2 shows the stress-strain curves of graphene and BN when loaded along the armchair and the zigzag directions. Sudden drops in the stress-strain curves indicate the ultimate fracture of the samples. It can be noticed that the fracture strains of BN along both armchair and zigzag directions are almost identical, whereas the fracture strain of graphene along the zigzag direction is significantly higher than that of the armchair direction. The stress-strain curves for BN along armchair and zigzag directions slightly deviate from each other at higher strains, which can be characterized by defining an effective nonlinear (third-order) elastic modulus [61]. It can also be observed that the fracture stress of graphene and BN when it is loaded along the zigzag direction is approximately 8% higher than that of the armchair direction. This is due to the different bond arrangements along the two loading directions. When the samples are loaded along the armchair direction (see Fig 1(b)), numerous bonds are aligned along the loading direction and these bonds carry comparatively higher strain leading to a higher bond stress. In contrast, all the bonds are inclined to the loading direction when the samples are loaded along the zigzag direction (see Fig 1(c)) and a part of the applied strain is accommodated by altering the bond angles resulting a reduced bond strain. The MD simulation results of the current study are in good agreement with the existing literature as compared in Table 1.

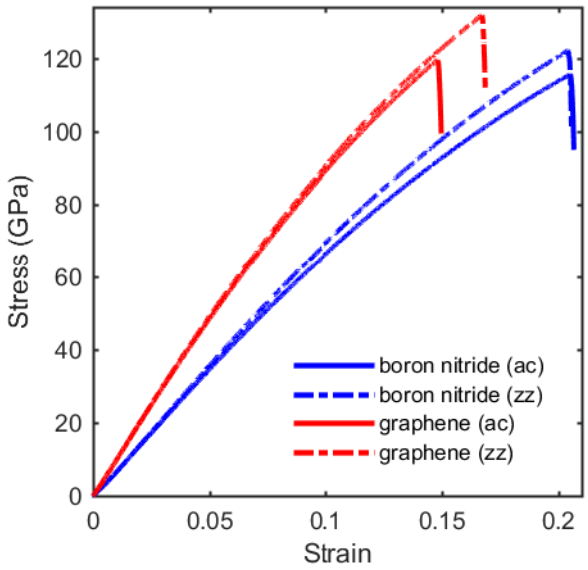

Figure 2 Stress-strain curves of pristine graphene and BN samples when loaded along the armchair (ac) and zigzag (zz) directions.

Table 1 Comparison of the current MD simulation results with the literature.

Material	Property	Reference/method	Value	Present study
Graphene	Young's modulus (TPa)	Lee et al. [62]/ Experiments	1 ± 0.15	1.00
		Liu et al. [63]/ DFT	1.05	
	Fracture stress (GPa)	Lee et al. [62]/ Experiments	123.5 ± 11.8	131 (zigzag)
		Liu et al. [63]/ DFT	121 (zigzag)	119(armchair)
			110 (armchair)	
BN	Young's modulus (TPa)	Sahin et al. [64]/ DFT	0.78	0.70
		Le and Umeno [34]/ MD	~0.73	
	Fracture stress (GPa)	Le and Umeno [34]/ MD	113 (zigzag)	122 (zigzag)
			102 (armchair)	115(armchair)

3.2 *Stress field near inclusions*

The stress states of individual atoms are useful in characterizing the crack-inclusion interaction of graphene. For example, the variations of the crack-tip atomic stress field in the presence of an inclusion at various locations relative to the crack-tip provide valuable information on the nature of the crack-inclusion interaction. In this section, the atomic stress distribution at a BN inclusion is investigated.

Figure 3(a) shows the simulated graphene sample containing a circular BN inclusion with a diameter of 10 nm. The BN inclusion does not generate a significant eigenstrain in the sample due to the fact that the lengths of both C-C and B-N bonds are 1.44 Å according to the Tersoff potential [34]. Moreover, the stress distribution within the inclusion is constant (see Fig. 3(c)). This observation agrees with the Eshelby theory [14,65], which states that a uniformly applied far-field stress induces a constant stress state within the inclusion. A complex stress state is observed at the graphene-BN interface, where the atomic stress ranges from 0 to 35 GPa due to a uniform far-field stress of 20 GPa. This complex stress distribution is attributed to (a) heterogeneous atomic bonds at the interface and (b) the change of chirality along the graphene-BN interface. The inter-atomic bonds within the BN inclusion and the surrounding graphene sheet are B-N and C-C, respectively. However, atoms at the BN-graphene interface form four types of atomic bonds; namely, B-C, N-C, B-N, and C-C bonds. This highly heterogeneous bond arrangement at the interface contributes to the observed complex stress state. In addition, chirality of the interface gradually changes from armchair to zigzag when the angle β (see Fig. 3(c)) increases from 0 to $\pi/6$ [21]. The chirality further changes gradually back to zigzag when β further increases from $\pi/6$ to $\pi/3$. This change in the underlying crystal structure along the interface also results in a complex stress state at the interface. Figure 3(d)

shows that the uniform stress field within the inclusion is approximately 17 GPa. In addition, a stress concentration of approximately 1.2 can be observed in graphene at the interface due to the relatively low elastic modulus of BN (see Table 1).

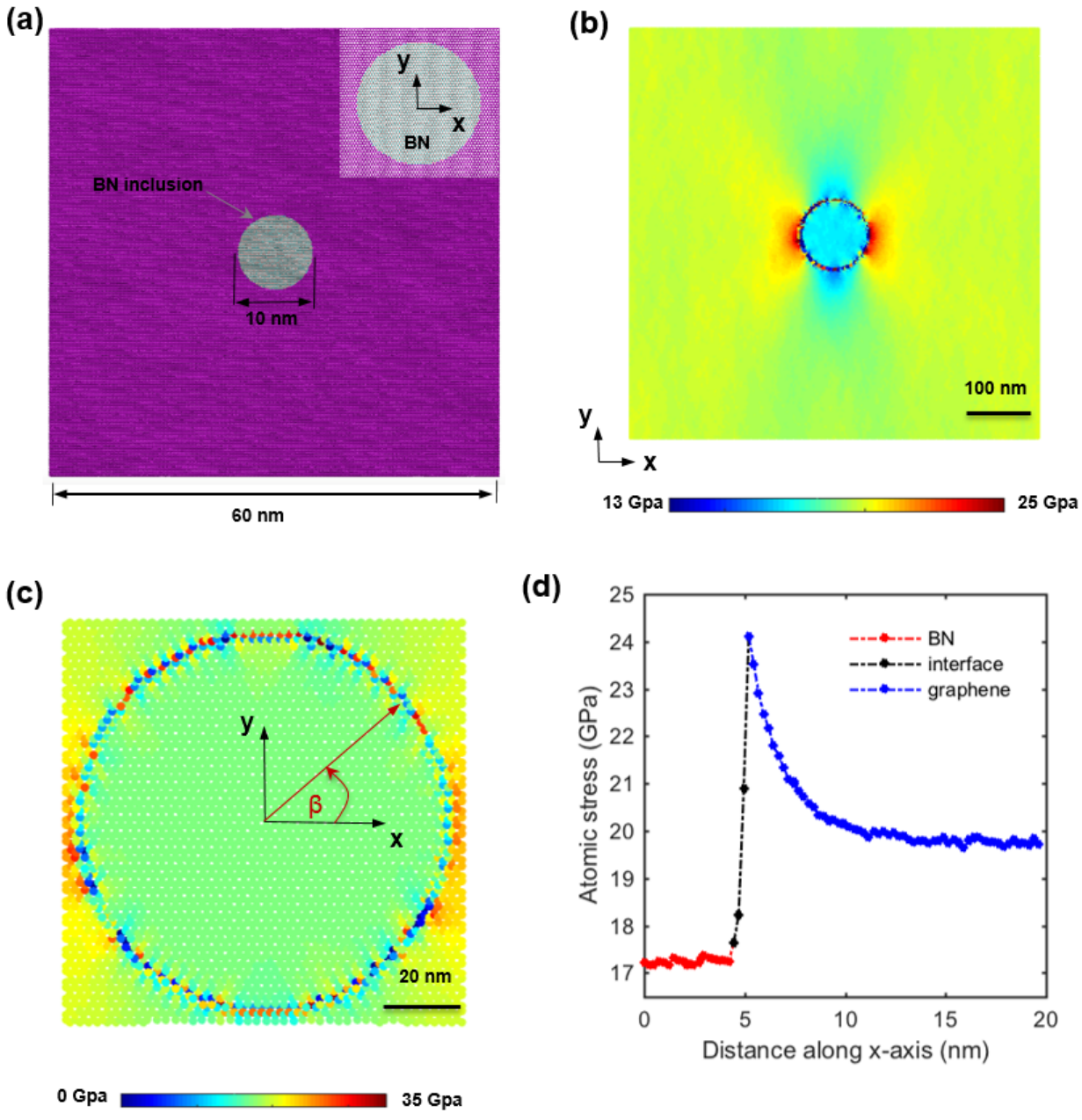

Figure 3 Stress field around a circular BN inclusion. (**a**) The simulated sample, where the inset demonstrates the selected origin of the Cartesian coordinate system. (**b**) and (**c**) show the stress σ_{yy} fields of the graphene sheet and the BN inclusion due to an applied tensile strain ε_{yy} of 2%. (**d**) Variation of the atomic stress σ_{yy} along the x-axis.

3.3 *Crack-inclusion interaction*

In continuum fracture mechanics, it is well established that inclusions in close proximity to a crack can lead to a considerable change in the crack-tip stress field [12–14,16]. However, it is unclear how nanoscale crack-inclusion interaction manifests itself at the atomistic level. In this section, we investigate the interaction between an atomistic edge crack and a circular BN inclusion in graphene.

We conducted numerical nanoscale uniaxial tensile tests of graphene samples containing an edge crack and a circular inclusion or a hole (see Fig. 1a) in order to investigate the influence of these inhomogeneities on the resulting stress field ahead of the crack-tip. The stress σ_{yy} distribution at the armchair crack-tip due to an applied tensile strain ε_{yy} of 1% is shown in Fig. 4. The figure clearly depicts that holes have a greater influence on the crack-tip stress field compared to the inclusion. Depending on the relative positions of the inclusion with respect to the crack-tip, the inclusions can result in a decrease of the crack-tip stress field (shielding effect) or an increase of the crack-tip stress field (amplification effect). However, in the case of interacting holes, the corresponding shielding and amplification effects are significantly higher than the effects induced by the inclusions. The shielding and amplification of the crack-tip stress field is due to the fact that the presence of inclusions results in reorienting the path of the stress trajectories and that could lead an increase (amplification) or decrease (shielding) of the density of the force lines that govern the stress trajectories at the crack-tip. Comparing Figs. 4(a) and

4(b), it can be seen that the interaction between the stress fields created by the crack and the inclusion in Fig. 4(b) is negligible, when the interference distance r is 6.8 nm, and the stress at the crack-tip reaches the stress value of an isolated crack (61.5 GPa). However, even at this interference distance, the hole demonstrates a significant interaction with the crack-tip stress field. A similar observation was made in the case of the zigzag crack. However, the atomic configurations of the zigzag crack-tip results in a slightly higher amplification effect compared to the armchair crack.

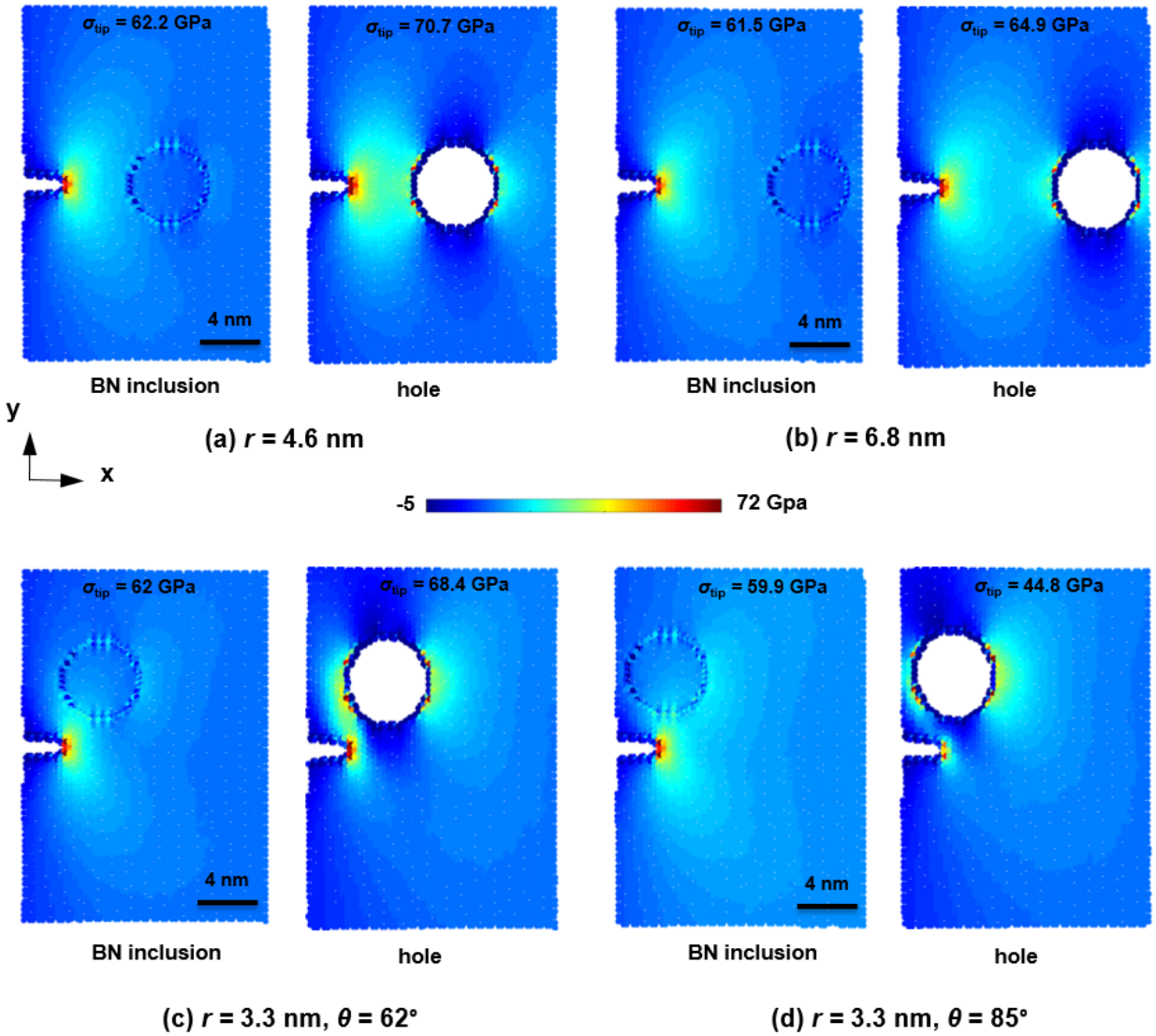

Figure 4 The stress σ_{yy} distribution at the armchair crack-tip due to an applied tensile strain ε_{yy} of 1% in the presence of an inclusion or a hole at various special locations identified by r and θ: (**a**) and (**b**) are for collinear inclusions/holes, i.e. $\theta = 0$. (**c**) and (**d**) are for oblique inclusions/holes. Considering symmetry, one half of the examined geometry is depicted. Noting that σ_{tip} is the stress at the crack-tip.

According to linear elastic fracture mechanics, the critical stress intensity factor (SIF) of a single edge-cracked sample under mode-I loading K_{IC} can be defined as follows [66]:

$$K_{IC} = 1.12\sigma_f\sqrt{\pi a} \ , \tag{5}$$

where a is the initial crack length, and σ_f is the fracture stress, i.e. the far field stress at the crack propagation. The computed K_{IC} for armchair and zigzag cracks are 4.66 and 4.44 MPa√m, respectively, which are in good agreement with the experimentally measured value of 4 MPa√m [67]. It should also be noted that the samples, used for the experiment, contained a central crack, where $K_{IC} = \sigma_f\sqrt{\pi a}$ and a is the half initial crack length of the central crack.

In the absence of the inclusion, the singular stress field near the crack-tip can be characterized by the corresponding SIF $K_I = 1.12\sigma_0\sqrt{\pi a}$ where σ_0 is the far field stress. However, the presence of the BN inclusion at the crack-tip influences the crack-tip stress field leading to a different SIF defined to be $K_I^{C\text{-}BN}$ in this study. The new SIF can be given as

$$K_I^{C-BC} = K_I + \Delta K_I \ , \tag{6}$$

where ΔK_I considers the stress disturbance due to the presence of the inclusion. Using the concepts of transformation toughening [68,69], Li et al. developed a general solution for the stress disturbance due to the interaction between a crack and an inclusion under plane stress mode I loading [16]. According to their solution, the change in crack-tip SIF can be expressed as

$$\Delta K_{\mathrm{I}} = \frac{K_{\mathrm{I}}}{2\pi}\int_{\Omega} r^{-2}\left(C_1 \cos\left(\frac{\theta}{2}\right)\cos\left(\frac{3\theta}{2}\right) + C_2 \sin^2(\theta)\cos(\theta)\right) d\Omega\,, \tag{7}$$

where r, θ, and Ω are define in Fig. 5(a). The constant C_1 and C_2 are given as

$$C_1 = \frac{(1-\alpha)(1-\nu)}{1+\alpha-\nu+\alpha\nu} \quad \text{and} \quad C_2 = \frac{(1-\alpha)(1+\nu)}{1+3\alpha+\nu-\alpha\nu} \tag{8}$$

Where ν is the Poisson's ratio which was assumed to be the same for the inclusion and matrix material; $\alpha = E_i/E_m$, where E_i and E_m are Young's moduli of inclusion and matrix, respectively.

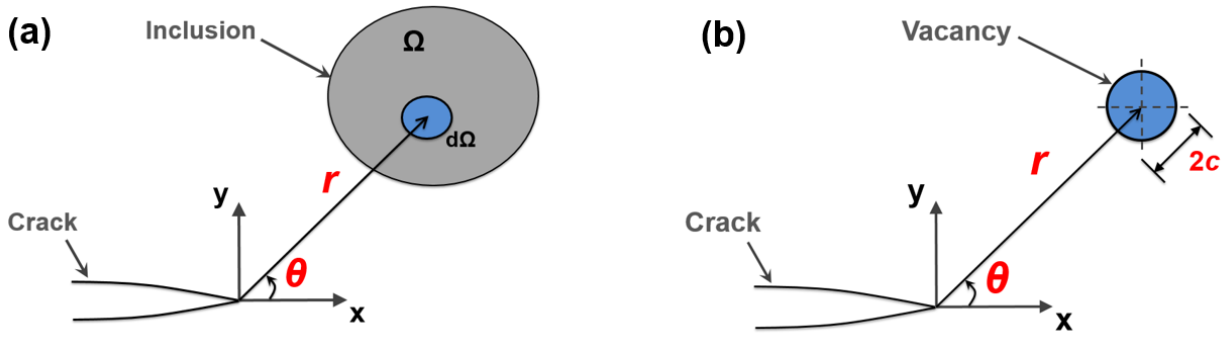

Figure 5 Relative locations of: (**a**) inclusion and (**b**) hole located near the tip of an edge crack.

Considering the case of an interacting inclusion located near the tip of a crack, the solution for the normalized SIF under mode I loading $K_{\mathrm{I}}^{\mathrm{C-BN}}/K_{\mathrm{I}}$ can be explicitly expressed as follows:

$$\frac{K_{\mathrm{I}}^{\mathrm{C-BN}}}{K_{\mathrm{I}}} = 1 + \frac{1}{2\pi}\int_{\Omega} r^{-2}\left(C_1 \cos\left(\frac{\theta}{2}\right)\cos\left(\frac{3\theta}{2}\right) + C_2 \sin^2(\theta)\cos(\theta)\right) d\Omega\,, \tag{9}$$

Earlier, Gong and Meguid studied the interaction between a semi-infinite crack and a circular hole located near its tip (see Fig. 5(b)) under mode I loading [70]. They analyzed the problem using the complex potentials of Muskhelishvili [71] and an appropriate superposition procedure

and obtained a closed-form solution for $K_{\mathrm{I}}^{(\mathrm{C\text{-}H})}$, which is the corresponding stress intensity factor in the presence of an interacting vacancy. According to their work, when a collinear circular hole is located ahead of the main crack, i.e. $\theta = 0$, the solution for the normalized stress intensity factor under mode I loading $K_{\mathrm{I}}^{(\mathrm{C\text{-}H})}/ K_{\mathrm{I}}$ can be explicitly expressed up to the order $(c/r)^4$ as follows:

$$\frac{K_{\mathrm{I}}^{(\mathrm{C\text{-}H})}}{K_{\mathrm{I}}} = 1 + \left(\frac{1}{2}\right)\left(\frac{c}{r}\right)^2 + \left(\frac{1}{4}\right)\left(\frac{c}{r}\right)^4 + \cdots \tag{10}$$

Considering the leading order solution up to the order $(c/r)^2$, an analytical expression for the normalized stress intensity factor $K_{\mathrm{I}}^{(\mathrm{C\text{-}H})}/ K_{\mathrm{I}}$ for a general case, i.e. for any combination of r and θ, can be given as

$$\frac{K_{\mathrm{I}}^{(\mathrm{C\text{-}H})}}{K_{\mathrm{I}}} = 1 + \left(\frac{c}{\sqrt{2}r}\right)^2 \cos\left(\frac{3\theta}{2}\right)\cos\left(\frac{\theta}{2}\right). \tag{11}$$

In order to characterize the crack-inclusion interaction, we used the normalized crack-tip stress $\sigma_{\mathrm{tip}}^{\mathrm{C-BN}}/\sigma_{\mathrm{tip}}$, where $\sigma_{\mathrm{tip}}^{\mathrm{C-BN}}$ and σ_{tip} are the crack-tip stresses along the y-direction in the presence of and in the absence of an interacting inclusion, respectively. The normalized crack-tip stress $\sigma_{\mathrm{tip}}^{\mathrm{C-BN}}/\sigma_{\mathrm{tip}}$ was computed at an applied tensile strain $\varepsilon_{\mathrm{yy}}$ level of 1% for various arrangements of the interacting inclusions. The values of σ_{tip} for the armchair and zigzag cracks are 61.5 and 64.9 GPa, respectively. Figures 6(a) and 6(b) reveal that the BN inclusions have significantly different influence on the crack-tip stress fields of zigzag and armchair cracks. This difference in the crack-tip stress field is due to the difference in the underlying crystal structures at the crack-tips of both cases (see Fig. 1(a) and 1(b)). It can be seen in Fig. 6(a) that the collinear (i.e. $\theta = 0°$) inclusions result in amplification of the crack-tip stress field

(i.e. $\sigma_{\mathrm{tip}}^{\mathrm{C-BN}}/\sigma_{\mathrm{tip}} > 1$). Inclusions with the oblique angle $\theta > 90°$ (see Fig. 6(b)), result in a shielding of the crack-tip stress field (i.e. $\sigma_{\mathrm{tip}}^{\mathrm{C-BN}}/\sigma_{\mathrm{tip}} < 1$).

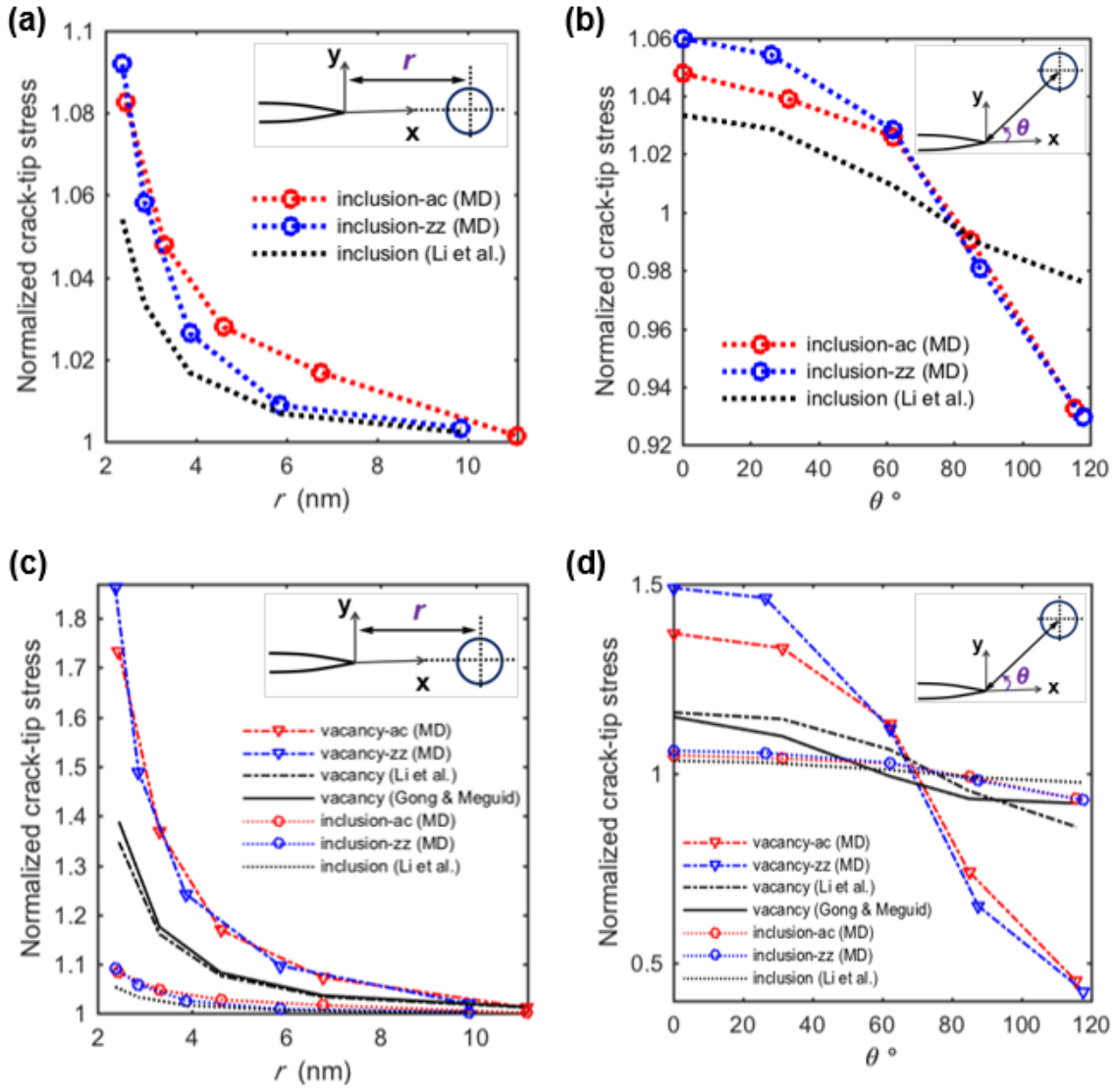

Figure 6 The effect of the BN inclusions on the crack-tip stress field: (**a**) and (**b**) show the variation of the normalized crack-tip stress $\sigma_{\mathrm{tip}}^{\mathrm{C-BN}}/\sigma_{\mathrm{tip}}$with r and θ, where Fig. 6(a) is for the collinear inclusions (θ = 0°) and Fig. 6(b) for the oblique inclusions (r is 2.8 and 3.3 nm for the zigzag and armchair cracks, respectively). Insets depict the location of the BN inclusion with respect to the crack-tip. (**c**) and (**d**) compare the crack-inclusion interactions with the

corresponding crack-hole interactions. Insets depict the location of the corresponding inclusion/hole with respect to the crack-tip.

Figures 6(a) and 6(b) also show that the continuum-based analytical solutions derived by Li et al., given in Eq. (9), captures the trends of the crack-tip stress fields obtained from our numerical experiments. Here, $K_{\mathrm{I}}^{\mathrm{C-BN}}/K_{\mathrm{I}}$ computed from Eq. (9) is compared with $\sigma_{\mathrm{tip}}^{\mathrm{C-BN}}/\sigma_{\mathrm{tip}}$ obtained from the MD simulations, where the analytical expression in Eq. (9) was solved numerically by taking into consideration the discrete nature of the atoms. The discretized form of Eq. (9) can be expressed as:

$$\frac{K_{\mathrm{I}}^{\mathrm{C-BN}}}{K_{\mathrm{I}}} = 1 + \frac{\mathrm{A_{bn}}}{2\pi}\sum_{n=1}^{N} r_n^{-2}\left(C_1 \cos\left(\frac{\theta_n}{2}\right)\cos\left(\frac{3\theta_n}{2}\right) + C_2 \sin^2(\theta_n)\cos(\theta_n)\right) \tag{12}$$

where, $\mathrm{A_{bn}}$ is the representative area of boron and nitrogen atoms in unstrained BN and the atomic inclusion contains N atoms, r_n is the distance between the tip of the crack and the atom n in the inclusion, and θ_n is the inclination angle between the x-axis and the line joining the tip of the crack and the atom n. The quantities r_n and θ_n resemble the r and θ depicted in Fig. 5(b).

The normalized crack-tip stress $\sigma_{\mathrm{tip}}^{\mathrm{C-BN}}/\sigma_{\mathrm{tip}}$ is comparable to the corresponding normalized stress intensity factor [24,66]. Figures 6(c) and 6(d) compare the crack-inclusion interaction with the corresponding crack-hole interaction. The figures clearly show that the influence of inclusions on the crack-tip stress field is practically negligible when it is compared with the influence of holes. As shown Figs. 6(a) and 6(b), the inclusions result in stress shielding or amplification effects of approximately 7% and 10%, respectively. The corresponding shielding and amplification effects due to the holes are well above 50%. Moreover, in Figs. 6(c) and 6(d), the crack-hole interaction results obtained from MD simulations were compared with the continuum-based analytical solutions of Li et al. (Eq. (12)) and Gong and Meguid (Eq. (10)

and (11)). It can be noted that the continuum models significantly under predict the influence of holes. However, the accuracy of the analytical expressions improve when the ratio (c/r) decreases [16]. Figure 7 compares the two continuum models with the results of MD simulations for the case of colinear holes with a diameter of ~1.2 nm located ahead of an armchair crack and a zigzag crack. In Fig. 7, a better agreement can be observed between the MD simulations and the continuum models especially for the case of zigzag crack. Moreover, the analytical solution from Gong and Meguid is much closer to the MD simulations owing to the fact that their model was specifically developed for the crack-hole interactions. The discrepancy of the results obtained from MD simulations and continuum models can be attributed to the discrete nature of the matter and the surface effects at the nanoscale [17–20].

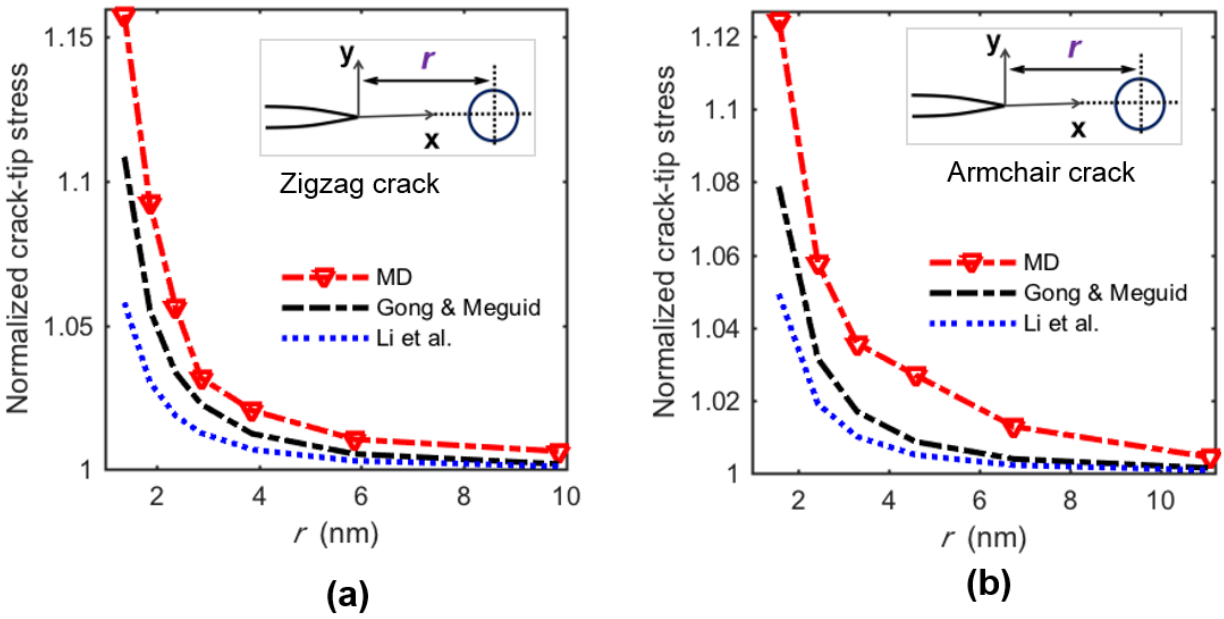

Figure 7 Comparison of the stress amplification results obtained from continuum models with the corresponding MD simulation result for (**a**) a zigzag crack and (**b**) an armchair crack. Insets depict the location of the hole with respect to the crack-tip.

It should be noted that the stress filed at the crack-tip is complex [23–25]. In fact, at finite temperatures, instantaneous atomic stress σ_{yy} at the crack-tip exhibits significantly high temporal fluctuations. In order to smooth these fluctuations out, we have averaged the instantaneous stress over sufficiently long time segments, as explained in section 2. As an alternative metric for the crack-tip stress σ_{yy}, the atomistic J integral can be employed to characterize the crack-inclusion interaction. Time averaged atomic field data obtained from MD simulations at finite temperatures can be used to compute the J integral [57,72,73].

Furthermore, our study reveals that the continuum-based models are incapable of predicting the influence of the underlying crystal structures (e.g., armchair versus zigzag) on the crack-tip stress field. Clearly, this sets a limit on developing a unified continuum fracture mechanics framework for atomic structures. However, due to the remarkable accuracy and the high computational efficiency, the analytical solutions can be used to develop design envelopes to ascertain the crack-tip shielding and amplification zones associated with the presence of inclusions ahead of the crack-tip in graphene. Earlier, Dewapriya and Meguid developed such design envelopes for crack-hole interactions using atomic simulations [24]. The analytical model due to Li et al. [16] can be employed to develop a comprehensive set of design envelops for the atomic-scale crack-inclusion interactions. Figure 8 shows two design envelops depicting the influence of atomic inclusions on the crack-tip stress field of an armchair crack for two modulus ratios (i.e. E_i/E_m). The envelopes clearly demonstrate that the regions associated with the stress shielding and amplification depend on the relative elastic modulus of the inclusion. When the elastic modulus of inclusion is smaller than the modulus of matrix material ($E_i/E_m < 1$), the inclusion predominantly introduces stress amplification (see Fig. 8a). In contrast,

when $E_i/E_m > 1$, the inclusion predominantly introduces stress shielding (Fig. 8b). In addition to the modulus ratio, the relative position of the inclusion with respect to the crack-tip also has a significant influence on the magnitude of stress shielding and amplification.

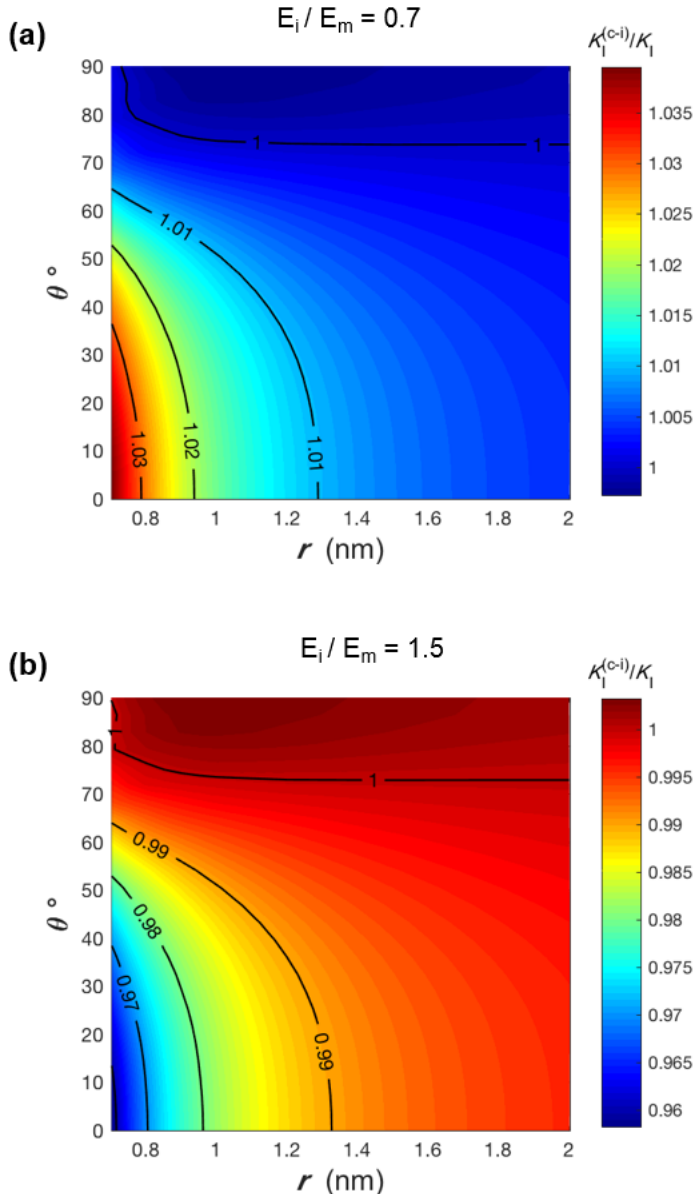

Figure 8 Design envelops depicting the influence of atomic inclusions on the crack-tip stress field of an armchair crack: (**a**) $E_i/E_m = 0.7$, which corresponds to a BN inclusion in graphene and (**b**) $E_i/E_m = 1.5$. Diameter of the inclusion is 1.2 nm. The quantities r and θ are as defined in figure 1(a).

3.4 *Fracture characterization*

In this section, we further characterize the atomistic crack-inclusion interaction by computing the critical SIF for the crack-inclusion arrangements considered in Fig. 6. The normalized critical SIF is defined to be $K_{\mathrm{IC}}^{\mathrm{C-BN}}/K_{\mathrm{IC}}$, where $K_{\mathrm{IC}}^{\mathrm{C-BN}}$ is the critical mode I SIF of a sample defined as

$$K_{\mathrm{IC}}^{\mathrm{C-BN}} = 1.12\sigma_{\mathrm{f}}^{\mathrm{C-BN}}\sqrt{\pi a}\,, \tag{13}$$

where $\sigma_{\mathrm{f}}^{\mathrm{C\text{-}BN}}$ is the fracture stress of the sample. It should be noted that $\sigma_{\mathrm{f}}^{\mathrm{C-BN}}$ obtained from MD simulations contains the influence of the interacting inclusion.

Figure 9 shows that the inclusions have led to a significant reduction in the fracture resistance of graphene, i.e. $K_{\mathrm{IC}}^{\mathrm{C-BN}}/K_{\mathrm{IC}} < 1$. This reduction is due to the fact that the inclusions influences the crack process zone and thus facilitating crack propagation. Particularly, the complex stress states at graphene-BN interface (see Fig. 3(c)) promotes crack growth. Moreover, the relatively low fracture toughness of BN, which is approximately 3.25 MPa√m [34], further enable the crack growth at a relatively low far field stress. Analogous to the observation made in Fig. 6, the inclusions have a greater influence on the fracture resistance of zigzag cracks when compared armchair cracks. However, the influence of BN inclusions on the fracture stress is negligible compared to the influence of holes. In the case of holes, special crack propagation mechanisms such as crack-hole coalescence lead to a significant increase in the critical SIF [24,25].

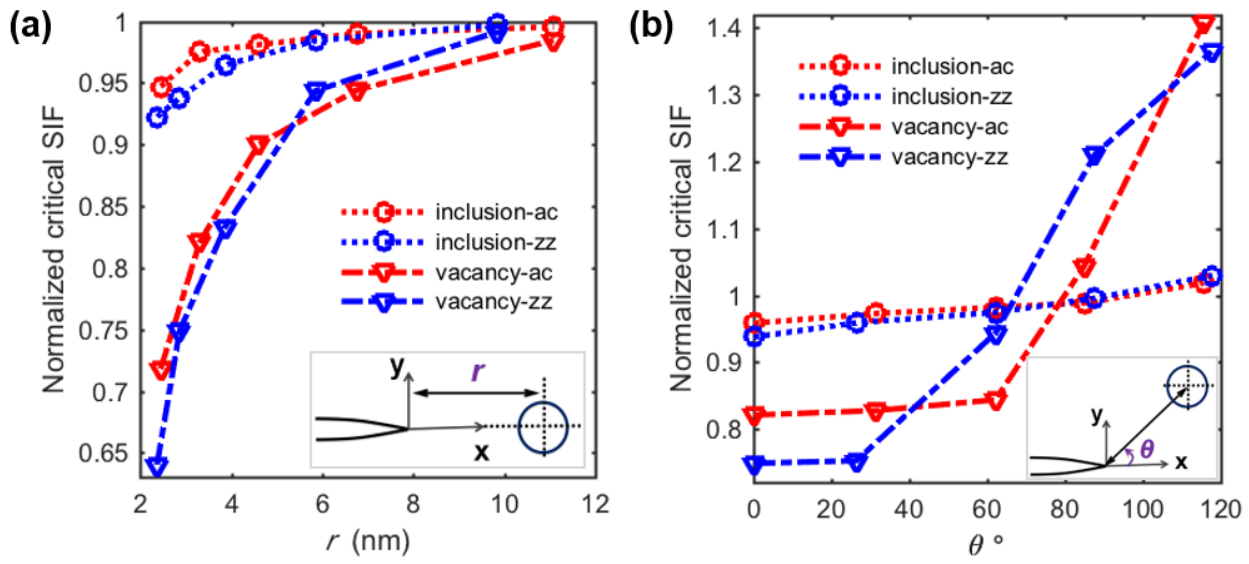

Figure 9 Variation of the normalized critical SIF $K_{\mathrm{IC}}^{\mathrm{C-BN}}/K_{\mathrm{IC}}$ of the considered crack-inclusion and crack-hole systems: (**a**) collinear inclusions/holes (θ = 0°), and (**b**) oblique inclusions/holes (r is 2.8 and 3.3 nm for the zigzag and armchair cracks, respectively). Insets depict the location of the corresponding inclusion/hole with respect to the crack-tip.

4. Conclusions

Our molecular dynamics simulations, complemented by a continuum-based analytical models, reveal that the crack-BN-inclusion interaction transforms the crack-tip stress field and the fracture strength of graphene providing another dimension in the design space of graphene-based hybrid materials. In addition to tailoring the physical properties of graphene-BN heterostructures by controlling the relative domain size of the inclusion, the presence of atomistic BN inclusions significantly influences the crack-tip stress field and the fracture resistance of graphene. For example, the atomic inclusions can lead to an increase in the crack-tip stress field by 11%; ultimately reducing the fracture strength by 8%. However, in the case of interacting atomic holes, the corresponding stress shielding and amplification are well above 50%. Our simulation

results elucidate the pronounced influence of the underlying crystal structure of two-dimensional materials on the crack-tip stress fields and their fracture resistance. In addition, we demonstrated that the continuum-based analytical solutions can be effectively used to develop comprehensive set of design envelopes to ascertain the crack-tip shielding and amplification zones associated with the presence of atomic inclusions ahead of the crack-tip. These findings significantly contribute to the existing knowledge concerning atomistic crack-inclusion interaction and the design of graphene-BN heterostructures with tunable electromechanical properties.

Acknowledgements

The authors thank NSERC for supporting this research. Computing resources were provided by WestGrid and Compute/Calcul Canada.

References

[1] F. Banhart, J. Kotakoski, A.V. Krasheninnikov, Structural Defects in Graphene, ACS Nano. 5 (2011) 26–41. doi:10.1021/nn102598m.

[2] A. Eichler, J. Moser, J. Chaste, M. Zdrojek, I. Wilson-Rae, A. Bachtold, Nonlinear damping in mechanical resonators made from carbon nanotubes and graphene., Nat Nanotechnol. 6 (2011) 339–342. doi:10.1038/nnano.2011.71.

[3] C. Chen, S. Rosenblatt, K.I. Bolotin, W. Kalb, P. Kim, I. Kymissis, H.L. Stormer, T.F. Heinz, J. Hone, Performance of monolayer graphene nanomechanical resonators with electrical readout, Nat. Nanotechnol. 4 (2009) 861–867. doi:10.1038/nnano.2009.267.

[4] L.G. Cançado, A. Jorio, E.H.M. Ferreira, F. Stavale, C.A. Achete, R.B. Capaz, M.V.O. Moutinho, A. Lombardo, T.S. Kulmala, A.C. Ferrari, Quantifying Defects in Graphene via Raman Spectroscopy at Different Excitation Energies, Nano Lett. 11 (2011) 3190–3196. doi:10.1021/nl201432g.

[5] A. Eckmann, A. Felten, A. Mishchenko, L. Britnell, R. Krupke, K.S. Novoselov, C. Casiraghi, Probing the Nature of Defects in Graphene by Raman Spectroscopy, Nano Lett. 12 (2012) 3925–3930. doi:10.1021/nl300901a.

[6] A. Kınacı, J.B. Haskins, C. Sevik, T. Çağın, Thermal conductivity of BN-C nanostructures, Phys. Rev. B. 86 (2012) 115410. doi:10.1103/PhysRevB.86.115410.

[7] L. Song, Z. Liu, A.L.M. Reddy, N.T. Narayanan, J. Taha-Tijerina, J. Peng, G. Gao, J. Lou, R. Vajtai, P.M. Ajayan, Binary and Ternary Atomic Layers Built from Carbon, Boron, and Nitrogen, Adv. Mater. 24 (2012) 4878–4895. doi:10.1002/adma.201201792.

[8] K. Yang, Y. Chen, R. D'Agosta, Y. Xie, J. Zhong, A. Rubio, Enhanced thermoelectric properties in hybrid graphene/boron nitride nanoribbons, Phys. Rev. B. 86 (2012) 045425. doi:10.1103/PhysRevB.86.045425.
[9] F. Banhart, J. Kotakoski, A.V. Krasheninnikov, Structural Defects in Graphene, ACS Nano. 5 (2011) 26–41. doi:10.1021/nn102598m.
[10] T. Zhang, X. Li, H. Gao, Fracture of graphene: a review, Int. J. Fract. (2015) 1–31. doi:10.1007/s10704-015-0039-9.
[11] M.A.N. Dewapriya, R.K.N.D. Rajapakse, Development of a homogenous nonlinear spring model characterizing the interfacial adhesion properties of graphene with surface defects, Compos. Part B Eng. 98 (2016) 339–349. doi:10.1016/j.compositesb.2016.04.052.
[12] T. Fett, E. Diegele, G. Rizzi, Calculation of stress fields near inclusions by use of the fracture mechanics weight function, Eng. Fract. Mech. 53 (1996) 17–22. doi:10.1016/0013-7944(95)00081-6.
[13] J. Helsing, Stress intensity factors for a crack in front of an inclusion, Eng. Fract. Mech. 64 (1999) 245–253. doi:10.1016/S0013-7944(99)00061-2.
[14] Z. Li, Q. Chen, Crack-inclusion interaction for mode I crack analyzed by Eshelby equivalent inclusion method, Int. J. Fract. 118 (2002) 29–40. doi:10.1023/A:1022652725943.
[15] S. Kumar, W.A. Curtin, Crack interaction with microstructure, Mater. Today. 10 (2007) 34–44. doi:10.1016/S1369-7021(07)70207-9.
[16] H. Li, J. Yang, Z. Li, An approximate solution for the plane stress mode I crack interacting with an inclusion of arbitrary shape, Eng. Fract. Mech. 116 (2014) 190–196. doi:10.1016/j.engfracmech.2013.12.010.
[17] L. Tapasztó, T. Dumitrică, S.J. Kim, P. Nemes-Incze, C. Hwang, L.P. Biró, Breakdown of continuum mechanics for nanometre-wavelength rippling of graphene, Nat. Phys. 8 (2012) 739–742. doi:10.1038/nphys2389.
[18] D.-B. Zhang, E. Akatyeva, T. Dumitrică, Bending Ultrathin Graphene at the Margins of Continuum Mechanics, Phys. Rev. Lett. 106 (2011). doi:10.1103/PhysRevLett.106.255503.
[19] H. Yin, H.J. Qi, F. Fan, T. Zhu, B. Wang, Y. Wei, Griffith Criterion for Brittle Fracture in Graphene, Nano Lett. 15 (2015) 1918–1924. doi:10.1021/nl5047686.
[20] L. Tian, R.K.N.D. Rajapakse, Elastic field of an isotropic matrix with a nanoscale elliptical inhomogeneity, Int. J. Solids Struct. 44 (2007) 7988–8005. doi:10.1016/j.ijsolstr.2007.05.019.
[21] M.A.N. Dewapriya, R.K.N.D. Rajapakse, N. Nigam, Influence of hydrogen functionalization on the fracture strength of graphene and the interfacial properties of graphene-polymer nanocomposite, Carbon. 1 (2015) 6991–7000. doi:10.1103/PhysRevB.37.6991.
[22] M.A.N. Dewapriya, R.K.N.D. Rajapakse, Molecular Dynamics Simulations and Continuum Modeling of Temperature and Strain Rate Dependent Fracture Strength of Graphene With Vacancy Defects, J. Appl. Mech. 81 (2014) 081010. doi:10.1115/1.4027681.
[23] M.A.N. Dewapriya, S.A. Meguid, Atomistic modeling of out-of-plane deformation of a propagating Griffith crack in graphene, Acta Mech. 228 (2017) 3063–3075. doi:10.1007/s00707-017-1883-7.
[24] M.A.N. Dewapriya, S.A. Meguid, Atomistic simulations of nanoscale crack-vacancy interaction in graphene, Carbon. 125 (2017) 113–131. doi:10.1016/j.carbon.2017.09.015.
[25] M.A.N. Dewapriya, S.A. Meguid, Tailoring fracture strength of graphene, Comput. Mater. Sci. 141 (2018) 114–121. doi:10.1016/j.commatsci.2017.09.005.
[26] L. Song, L. Ci, H. Lu, P.B. Sorokin, C. Jin, J. Ni, A.G. Kvashnin, D.G. Kvashnin, J. Lou, B.I. Yakobson, P.M. Ajayan, Large Scale Growth and Characterization of Atomic Hexagonal Boron Nitride Layers, Nano Lett. 10 (2010) 3209–3215. doi:10.1021/nl1022139.

[27] Y. Shi, C. Hamsen, X. Jia, K.K. Kim, A. Reina, M. Hofmann, A.L. Hsu, K. Zhang, H. Li, Z.-Y. Juang, M.S. Dresselhaus, L.-J. Li, J. Kong, Synthesis of Few-Layer Hexagonal Boron Nitride Thin Film by Chemical Vapor Deposition, Nano Lett. 10 (2010) 4134–4139. doi:10.1021/nl1023707.
[28] Y. Kubota, K. Watanabe, O. Tsuda, T. Taniguchi, Deep Ultraviolet Light-Emitting Hexagonal Boron Nitride Synthesized at Atmospheric Pressure, Science. 317 (2007) 932–934. doi:10.1126/science.1144216.
[29] J. Wu, B. Wang, Y. Wei, R. Yang, M. Dresselhaus, Mechanics and Mechanically Tunable Band Gap in Single-Layer Hexagonal Boron-Nitride, Mater. Res. Lett. 1 (2013) 200–206. doi:10.1080/21663831.2013.824516.
[30] Z. Liu, L. Ma, G. Shi, W. Zhou, Y. Gong, S. Lei, X. Yang, J. Zhang, J. Yu, K.P. Hackenberg, A. Babakhani, J.-C. Idrobo, R. Vajtai, J. Lou, P.M. Ajayan, In-plane heterostructures of graphene and hexagonal boron nitride with controlled domain sizes, Nat. Nanotechnol. 8 (2013) 119–124. doi:10.1038/nnano.2012.256.
[31] J. Wang, F. Ma, M. Sun, Graphene, hexagonal boron nitride, and their heterostructures: properties and applications, RSC Adv. 7 (2017) 16801–16822. doi:10.1039/C7RA00260B.
[32] A. Lopez-Bezanilla, S. Roche, Embedded boron nitride domains in graphene nanoribbons for transport gap engineering, Phys. Rev. B. 86 (2012) 165420. doi:10.1103/PhysRevB.86.165420.
[33] S. Zhao, J. Xue, Mechanical properties of hybrid graphene and hexagonal boron nitride sheets as revealed by molecular dynamic simulations, J. Phys. Appl. Phys. 46 (2013) 135303. doi:10.1088/0022-3727/46/13/135303.
[34] M.-Q. Le, Y. Umeno, Fracture of monolayer boronitrene and its interface with graphene, Int. J. Fract. 205 (2017) 151–168. doi:10.1007/s10704-017-0188-0.
[35] Z. Yu, M.L. Hu, C.X. Zhang, C.Y. He, L.Z. Sun, J. Zhong, Transport Properties of Hybrid Zigzag Graphene and Boron Nitride Nanoribbons, J. Phys. Chem. C. 115 (2011) 10836–10841. doi:10.1021/jp200870t.
[36] Y. Ding, Y. Wang, J. Ni, Electronic properties of graphene nanoribbons embedded in boron nitride sheets, Appl. Phys. Lett. 95 (2009) 123105. doi:10.1063/1.3234374.
[37] Q. Peng, A.R. Zamiri, W. Ji, S. De, Elastic properties of hybrid graphene/boron nitride monolayer, Acta Mech. 223 (2012) 2591–2596. doi:10.1007/s00707-012-0714-0.
[38] N. Ding, X. Chen, C.-M.L. Wu, Mechanical properties and failure behaviors of the interface of hybrid graphene/hexagonal boron nitride sheets, Sci. Rep. 6 (2016). doi:10.1038/srep31499.
[39] N. Ding, Y. Lei, X. Chen, Z. Deng, S.-P. Ng, C.-M.L. Wu, Structures and electronic properties of vacancies at the interface of hybrid graphene/hexagonal boron nitride sheet, Comput. Mater. Sci. 117 (2016) 172–179. doi:10.1016/j.commatsci.2015.12.052.
[40] F. Cleri, S.R. Phillpot, D. Wolf, S. Yip, Atomistic Simulations of Materials Fracture and the Link between Atomic and Continuum Length Scales, J. Am. Ceram. Soc. 81 (1998) 501–516. doi:10.1111/j.1151-2916.1998.tb02368.x.
[41] P. Zhang, L. Ma, F. Fan, Z. Zeng, C. Peng, P.E. Loya, Z. Liu, Y. Gong, J. Zhang, X. Zhang, others, Fracture toughness of graphene, Nat. Commun. 5 (2014).
[42] H. Yin, H.J. Qi, F. Fan, T. Zhu, B. Wang, Y. Wei, Griffith Criterion for Brittle Fracture in Graphene, Nano Lett. 15 (2015) 1918–1924. doi:10.1021/nl5047686.
[43] J. Tersoff, New empirical-approach for the structure and energy of covalent systems, Phys. Rev. B. 37 (1988) 6991–7000. doi:10.1103/PhysRevB.37.6991.
[44] S. Plimpton, Fast parallel algorithms for short-range molecular dynamics, J Comput Phys. 117 (1995) 1–19. doi:10.1006/jcph.1995.1039.
[45] R. Kumar, G. Rajasekaran, A. Parashar, Optimised cut-off function for Tersoff-like potentials for a BN nanosheet: a molecular dynamics study, Nanotechnology. 27 (2016) 085706. doi:10.1088/0957-4484/27/8/085706.

[46] D.W. Brenner, O.A. Shenderova, J.A. Harrison, S.J. Stuart, B. Ni, S.B. Sinnott, A second-generation reactive empirical bond order (REBO) potential energy expression for hydrocarbons, J. Phys. Condens. Matter. 14 (2002) 783.
[47] O.A. Shenderova, D.W. Brenner, A. Omeltchenko, X. Su, L.H. Yang, Atomistic modeling of the fracture of polycrystalline diamond, Phys Rev B. 61 (2000) 3877–3888. doi:10.1103/PhysRevB.61.3877.
[48] K.G.S. Dilrukshi, M.A.N. Dewapriya, U.G.A. Puswewala, Size dependency and potential field influence on deriving mechanical properties of carbon nanotubes using molecular dynamics, Theor. Appl. Mech. Lett. 5 (2015) 167–172. doi:http://dx.doi.org/10.1016/j.taml.2015.05.005.
[49] B. Zhang, L. Mei, H. Xiao, Nanofracture in graphene under complex mechanical stresses, Appl. Phys. Lett. 101 (2012) 121915. doi:10.1063/1.4754115.
[50] T. Zhang, X. Li, S. Kadkhodaei, H. Gao, Flaw Insensitive Fracture in Nanocrystalline Graphene, Nano Lett. 12 (2012) 4605–4610. doi:10.1021/nl301908b.
[51] M.A.N. Dewapriya, Molecular dynamics study of effects of geometric defects on the mechanical properties of graphene, Department of Mechanical Engineering, University of British Columbia, 2012.
[52] T. Zhang, X. Li, H. Gao, Designing graphene structures with controlled distributions of topological defects: A case study of toughness enhancement in graphene ruga, Extreme Mech. Lett. 1 (2014) 3–8. doi:10.1016/j.eml.2014.12.007.
[53] F. Meng, C. Chen, J. Song, Lattice trapping and crack decohesion in graphene, Carbon. 116 (2017) 33–39. doi:10.1016/j.carbon.2017.01.091.
[54] A.R. Alian, S.A. Meguid, Hybrid molecular dynamics–finite element simulations of the elastic behavior of polycrystalline graphene, Int. J. Mech. Mater. Des. (2017). doi:10.1007/s10999-017-9389-y.
[55] M.A.N. Dewapriya, A.S. Phani, R.K.N.D. Rajapakse, Influence of temperature and free edges on the mechanical properties of graphene, Model. Simul. Mater. Sci. Eng. 21 (2013) 065017.
[56] D.H. Tsai, The virial theorem and stress calculation in molecular dynamics, J. Chem. Phys. 70 (1979) 1375–1382. doi:10.1063/1.437577.
[57] M.A.N. Dewapriya, R.K.N.D. Rajapakse, A.S. Phani, Atomistic and continuum modelling of temperature-dependent fracture of graphene, Int. J. Fract. 187 (2014) 199–212. doi:10.1007/s10704-014-9931-y.
[58] T. Ohta, Controlling the Electronic Structure of Bilayer Graphene, Science. 313 (2006) 951–954. doi:10.1126/science.1130681.
[59] S.I. Kundalwal, S.A. Meguid, G.J. Weng, Strain gradient polarization in graphene, Carbon. 117 (2017) 462–472. doi:10.1016/j.carbon.2017.03.013.
[60] W. Humphrey, A. Dalke, K. Schulten, VMD – Visual Molecular Dynamics, J. Mol. Graph. 14 (1996) 33–38.
[61] E. Cadelano, P.L. Palla, S. Giordano, L. Colombo, Nonlinear Elasticity of Monolayer Graphene, Phys Rev Lett. 102 (2009) 235502. doi:10.1103/PhysRevLett.102.235502.
[62] C. Lee, X. Wei, J.W. Kysar, J. Hone, Measurement of the Elastic Properties and Intrinsic Strength of Monolayer Graphene, Science. 321 (2008) 385–388. doi:10.1126/science.1157996.
[63] F. Liu, P. Ming, J. Li, *Ab initio* calculation of ideal strength and phonon instability of graphene under tension, Phys Rev B. 76 (2007) 064120. doi:10.1103/PhysRevB.76.064120.
[64] H. Şahin, S. Cahangirov, M. Topsakal, E. Bekaroglu, E. Akturk, R.T. Senger, S. Ciraci, Monolayer honeycomb structures of group-IV elements and III-V binary compounds: First-principles calculations, Phys. Rev. B. 80 (2009). doi:10.1103/PhysRevB.80.155453.

[65] J. Eshelby, The Determination of the Elastic Field of an Ellipsoidal Inclusion, and Related Problems | Proceedings of the Royal Society of London A: Mathematical, Physical and Engineering Sciences, (n.d.). http://rspa.royalsocietypublishing.org/content/241/1226/376 (accessed August 31, 2017).
[66] S.A. Meguid, Engineering fracture mechanics, Elsevier Applied Science ; Sole distributor in the USA and Canada, Elsevier Science Pub, London ; New York : New York, 1989.
[67] P. Zhang, L. Ma, F. Fan, Z. Zeng, C. Peng, P.E. Loya, Z. Liu, Y. Gong, J. Zhang, X. Zhang, others, Fracture toughness of graphene, Nat. Commun. 5 (2014).
[68] F.F. Lange, Transformation toughening, J. Mater. Sci. 17 (1982) 225–234. doi:10.1007/BF00809057.
[69] A.H. Heuer, F.F. Lange, M.V. Swain, A.G. Evans, Transformation Toughening: An Overview, J. Am. Ceram. Soc. 69 (1986) i–iv. doi:10.1111/j.1151-2916.1986.tb07400.x.
[70] S.X. Gong, S.A. Meguid, Microdefect interacting with a main crack: A general treatment, Int. J. Mech. Sci. 34 (1992) 933–945. doi:10.1016/0020-7403(92)90063-M.
[71] N.I. Muskhelishvili, Some basic problems of the mathematical theory of elasticity: fundamental equations, plane theory of elasticity, torsion and bending, 1977. http://dx.doi.org/10.1007/978-94-017-3034-1 (accessed April 19, 2017).
[72] R.E. Jones, J.A. Zimmerman, The construction and application of an atomistic J-integral via Hardy estimates of continuum fields, J. Mech. Phys. Solids. 58 (2010) 1318–1337. doi:10.1016/j.jmps.2010.06.001.
[73] R.E. Jones, J.A. Zimmerman, J. Oswald, T. Belytschko, An atomistic J-integral at finite temperature based on Hardy estimates of continuum fields, J. Phys. Condens. Matter. 23 (2011) 015002. doi:10.1088/0953-8984/23/1/015002.